IJMMM International Journal of Minerals, Metallurgy and Materials 矿物冶金与材料学报（英文版）

Compressive fatigue behavior and failure evolution of additive fiber-reinforced cemented tailings composites

Jiajian Li, Shuai Cao, Erol Yilmaz, and Yunpeng Liu

Cite this article as:
Jiajian Li, Shuai Cao, Erol Yilmaz, and Yunpeng Liu, Compressive fatigue behavior and failure evolution of additive fiber-reinforced cemented tailings composites, *Int. J. Miner. Metall. Mater.*, 29(2022), No. 2, pp. 345-355. https://doi.org/10.1007/s12613-021-2351-x

---

International Journal of Minerals, Metallurgy and Materials
Volume 29, Number 2, February 2022, Page 345
https://doi.org/10.1007/s12613-021-2351-x

Compressive fatigue behavior and failure evolution of additive fiber-reinforced cemented tailings composites

Jiajian Li[1,2], *Shuai Cao*[1,2)✉], *Erol Yilmaz*[3)✉], *and Yunpeng Liu*[4)]

1) School of Civil and Resources Engineering, University of Science and Technology Beijing, Beijing 100083, China
2) State Key Laboratory of High-Efficient Mining and Safety of Metal Mines of Ministry of Education, University of Science and Technology Beijing, Beijing 100083, China
3) Department of Civil Engineering, Geotechnical Division, Recep Tayyip Erdogan University, Fener, Rize TR53100, Turkey
4) State Key Laboratory of Silicate Materials for Architectures (Wuhan University of Technology), Wuhan 430070, China
(Received: 28 July 2021; revised: 6 September 2021; accepted: 8 September 2021)

Abstract: The ordinary cemented tailings backfill (CTB) is a cement-based composite prepared from tailings, cementitious materials, and water. In this study, a series of laboratory tests, including uniaxial compression, digital image correlation measurement, and scanning electron microscope characteristics of fiber-reinforced CTB (FRCTB), was conducted to obtain the uniaxial compressive strength (UCS), failure evolution, and microstructural characteristics of FRCTB specimens. The results show that adding fibers could increase the UCS values of the CTB by 6.90% to 32.76%. The UCS value of the FRCTB increased with the increase in the polypropylene (PP) fiber content. Moreover, the reinforcement effect of PP fiber on the CTB was better than that of glass fiber. The addition of fiber could increase the peak strain of the FRCTB by 0.39% to 1.45%. The peak strain of the FRCTB increased with the increase in glass fiber content. The failure pattern of the FRCTB was coupled with tensile and shear failure. The addition of fiber effectively inhibited the propagation of cracks, and the bridging effect of cracks by the fiber effectively improved the mechanical properties of the FRCTB. The findings in this study can provide a basis for the backfilling design and optimization of mine backfilling methods.

Keywords: cemented tailings backfill; uniaxial compressive strength; combined fiber reinforcement; digital image correlation; microstructural characteristics

1. Introduction

The underground backfilling technique has significant advantages in eliminating tailings on the surface and effectively controlling ground pressure [1–3]. Generally, backfilling materials are prepared using tailings, binder materials, and water, which are collectively called cemented tailings backfill (CTB) or cemented paste backfill (CPB). Many scholars and engineers have examined the mechanical characteristics and microstructures of CTB or CPB [4–6]. Results show that the mechanical properties of ordinary CTB or CPB were similar to those of concrete, but their toughness was poor [7–9]. On the one hand, the collapse of the CTB or CPB threatened the safety of mine workers and equipment. On the other hand, the collapse of the CTB or CPB could easily cause ore dilution when mixed into the mining stope [10–13]. The collapse of the filling body poses a serious threat to the safe production of mines. Thus, it is very necessary to improve the flexural and crack resistance of the backfill. Whether we can add fibers and other additives to prepare CTB specimens with high mechanical strength, good flexural, and crack resistance is the basis of the topic of this study.

Generally, the mechanical properties of the CTB or CPB are affected by several factors, including tailings type, solid content (SC), binder content and type, curing time, and curing temperature [14–22]. Furthermore, scholars and engineers have conducted considerable research on the improvement of the CTB or CPB performance [23–26]. Additive materials (AMs) can change the mechanical behavior of the CTB or CPB. Zhao *et al.* [27] found that adding a small amount (<20wt%) of steel slag to superfine CTB can improve the mechanical properties of the backfill. Liu *et al.* [28] found that the increase in sulfur content can slightly increase the strength of the CTB. Chen *et al.* [29] found that adding CaO to cemented composites made of cement, phosphogypsum, and phosphate tailings can greatly increase their compressive strength. In addition, some researchers found that by changing the internal structure of the CTB or CPB, the mechanical properties could be improved [30–32]. The addition of straw, fiber, and lattice structures in the CTB or CPB could increase the mechanical characteristics, including compression and flexural strength [33–35]. The bridging effect of the AM and hydration products inhibited the initiation and propagation of cracks in the CTB or CPB and improved

✉ Corresponding authors: Shuai Cao E-mail: sandy_cao@ustb.edu.cn; Erol Yilmaz E-mail: erol.yilmaz@erdogan.edu.tr

their mechanical properties [36]. Moreover, the reinforcement effect was closely related to the content and type of the AM [37–40]. However, studies have shown that straw or fiber could increase the ductility of the CTB or CPB but have some minor side effects. For example, the water absorption of rice straw and fiber adversely affects the fluidity of the CTB or CPB. Chen *et al.* [41] found that straw can reduce the fluidity of fresh CTB slurry by 5%.

Considerable research has been performed on fiber-reinforced CTB (FRCTB) or CPB. The present findings are mainly focused on the mechanical research of a single type of FRCTB or CPB. However, there is still no investigation on more than two different FRCTBs or CPBs until now. To explore the combined fiber-reinforced mechanism on the CTB, a series of laboratory tests, including uniaxial compressive test, digital image correlation (DIC), and scanning electron microscope (SEM), were conducted in this study. Glass fiber and polypropylene (PP) fiber were adopted to prepare the FRCTB specimens. The uniaxial compressive strength (UCS), peak strain, failure evolution, and microstructural parameters of the FRCTB were obtained. The findings can provide a reliable reference for underground backfilling designs in the future.

2. Experimental

2.1. Materials

2.1.1. Tungsten tailings, cement, and water mixture

In this study, the tungsten tailings from Yunnan, China, were used to prepare the CTB. Ordinary Portland cement (OPC) 42.5R from Tianjin, China, was added as the cementitious binder. The number 42.5 shows the minimum desired strength value achieved within 28 d. "R" indicates that the cement has early strength. Tap water was adopted to mix the solid compositions, including tailings and OPC 42.5R. Then, the chemical compositions of the tailings and OPC 42.5R were measured using a sequential X-ray fluorescence spectrometer from the University of Science and Technology Beijing (USTB), which are shown in Table 1. The results show that the main oxides in OPC 42.5R are calcium oxide (43.3wt%), silica (27.4wt%), and alumina (11.4wt%). Moreover, silica (31.3wt%), calcium oxide (28.2wt%), alumina (15.5wt%), and ferric oxide (13.0wt%) were the main oxides in the tested tailings sample.

Table 1. Chemical compositions of OPC 42.5R and tailings wt%

Sample	CaO	SiO_2	Al_2O_3	MgO	Fe_2O_3	SO_3	Na_2O	TiO_2	K_2O
OPC 42.5R	43.3	27.4	11.4	8.7	3.3	2.2	1.1	0.8	0.6
Tailings	28.2	31.3	15.5	6.8	13.0	1.5	1.5	1.1	1.3

In this study, the particle size distribution (PSD) of the tested tailings was measured using the laser particle size analyzer LS-POP, as shown in Fig. 1.

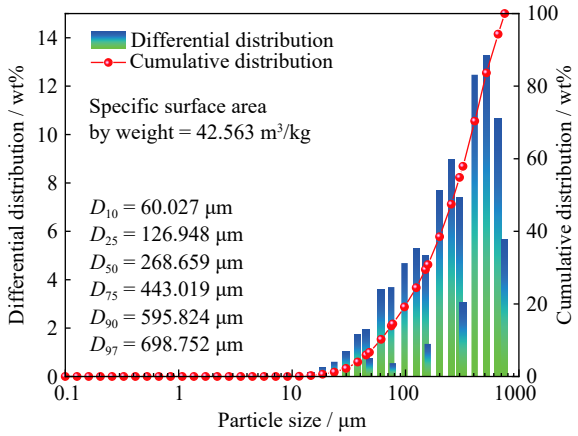

Fig. 1. Particle size distribution of tungsten tailings in this study.

The meaning of "D_{10}" is that the content of particles less than 60.027 μm account for 10wt%. The meanings of other parameters such as D_{25} and D_{50} are similar to D_{10}. The specific surface area was 42.563 m^3/kg, and the PSD of the tested tailings vary between 7.2 and 750 μm, with the vast majority sized between 407.8 and 655.8 μm. Thus, the tested tailings were rather coarse and had uneven PSD.

2.1.2. Polypropylene fiber and glass fiber

In this study, two types of fibers, namely, PP fiber and glass fiber, were adopted as AMs. To reduce the influence of interfering factors on the experiment results, the length of the above fibers was set to 12 mm. The density values and tensile strength values of the PP fiber were 0.91 g/cm^3 and 398 MPa, respectively, and those of the glass fiber were 2.02 g/cm^3 and 324 MPa, respectively. Moreover, the elongation rate values of the PP and glass fibers were 28.0% and 36.5%, respectively.

2.2. Preparation of the FRCTB specimens

The total amount of the glass and PP fibers in the CTB was 0.6wt%. To investigate the influence of the combined fibers on the mechanical properties of the CTB, eight groups of fiber combination experiments were set up. Table 2 shows the mixing ratios of the glass and PP fibers in this test. "G-0.6-PP-0.0" was taken as an example, where "G" represents

Table 2. Mixture proportions of FRCTB specimens used during the experiments wt%

Specimen ID	Glass fiber	Polypropylene fiber	Fiber content
G-0.0-PP-0.0	0.0	0.0	0.0
G-0.0-PP-0.6	0.0	0.6	0.6
G-0.1-PP-0.5	0.1	0.5	0.6
G-0.2-PP-0.4	0.2	0.4	0.6
G-0.3-PP-0.3	0.3	0.3	0.6
G-0.4-PP-0.2	0.4	0.2	0.6
G-0.5-PP-0.1	0.5	0.1	0.6
G-0.6-PP-0.0	0.6	0.0	0.6

the glass fiber; "0.6" is the additional amount of glass fiber, i.e., 0.6wt%; "PP" is the PP fiber, and "0.0" is the additional amount of PP fiber, i.e., 0.0wt%. The SC and cement-to-tailings ratio (c/t) were 70wt% and 1:6, respectively. First, the fried tailings and fibers were stirred for 180 s. Then, tap water was added and stirred for 180 s. The mixed slurry was poured into the cylindrical steel molds with a diameter of 50 mm and a height of 100 mm and immediately placed into a constant temperature (20±5)°C and humidity 95%±5% curing box. The FRCTB specimens were demolded after 48 h. The curing time was set to 3 and 7 d. Fig. 2 shows the preparation process of the FRCTB specimens.

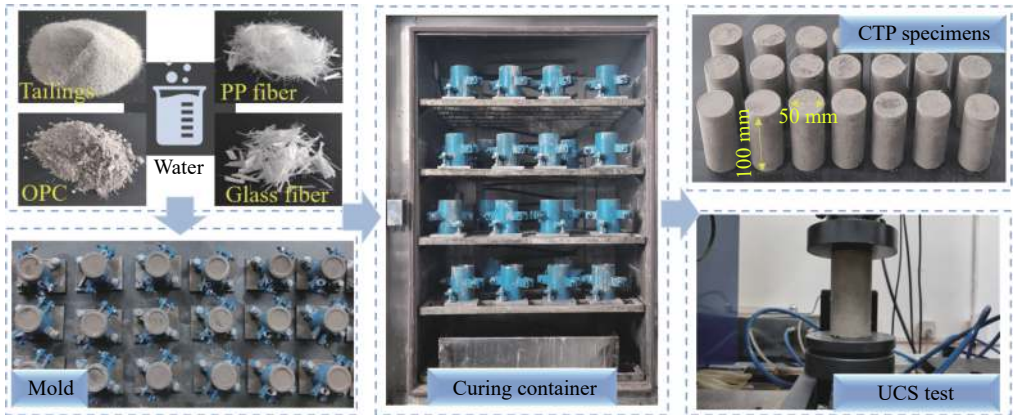

Fig. 2. Preparation processes of FRCTB specimens used during the experiments.

2.3. UCS testing with DIC

In this part, the uniaxial compression test was conducted using the computer-controlled uniaxial compressive testing system WDW-200D from the USTB. The tested FRCTB specimens were polished to ensure that their flatness was ±0.02 mm. The loading rate was set as 1.0 mm/min during the whole loading process. The load and displacement parameters can be saved and recorded on the computer in real-time.

A non-contact strain measurement system (SMS) was used to record the deformation process of the FRCTB specimen surfaces during the uniaxial compression experiment. The three-dimensional (3D) SMS and DIC techniques were adopted to track the speckle image of the object surface to achieve 3D strain results during the deformation process. The strain measurement range was between 0.005 and 2000%. Fig. 3 shows the principle of the uniaxial compression experiments using DIC technology.

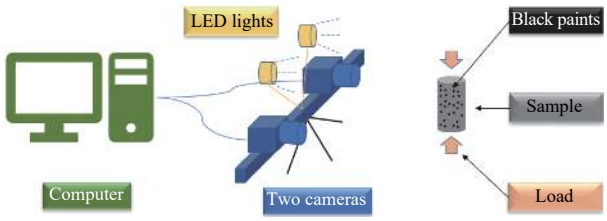

Fig. 3. Principle of uniaxial compression experiments using DIC technology.

During the laboratory test, the white paints and black spots should be sprayed on the surface of the FRCTB specimens, and two light-emitting diode (LED) lights should be set up above the camera. The camera was placed in front of the FRCTB specimens, approximately 1 m away from the specimen. The angle between the two cameras was between 15° and 30°. The camera took one picture every second during the whole loading process. The computer was used to control the camera and collect images. Moreover, the strain measurement area was the same area captured by the left and right cameras.

2.4. SEM and EDS tests

In this part, the SEM Zeiss EVO18 and X-ray energy-dispersive spectrometer were adopted to explore the microstructure of different FRCTB samples. The surfaces of the tested FRCTB samples were treated with carbon spray twice to enhance the conductivity of the SEM sample before the observation. Then, the prepared samples were placed into the vacuum chamber and evacuated. The acceleration voltage was 10–20 kV, the magnification was 50–2000, and the resolution was 3 nm.

3. Results and discussion

3.1. Effect of fiber content on the UCS

Fig. 4 shows the relationship among the specimen number, UCS, and UCS increment. The UCS value of non-FRCTB (NFRCTB) was 0.59 MPa, and the UCS values of the FRCTB specimens were between 0.49 and 0.67 MPa when the curing time was 3 d. Moreover, the strength change of the FRCTB was less than 0.1 MPa compared with the NFRCTB. The UCS increment values were between −16.95% and 13.56%. Hence, the glass and PP fibers had no evident enhancement effect on the UCS of the FRCTB, and the content change of the two fibers had no clear effect on the UCS of the CTB when the curing time was 3 d. The possible reason was that the hydration reaction in the CTB was insufficient within three days. The UCS of the FRCTB was the same as those of the NFRCTB specimens. However, the UCS value of the NFRCTB was 1.16 MPa when the curing time was 7 d. The UCS values of all the FRCTB specimens

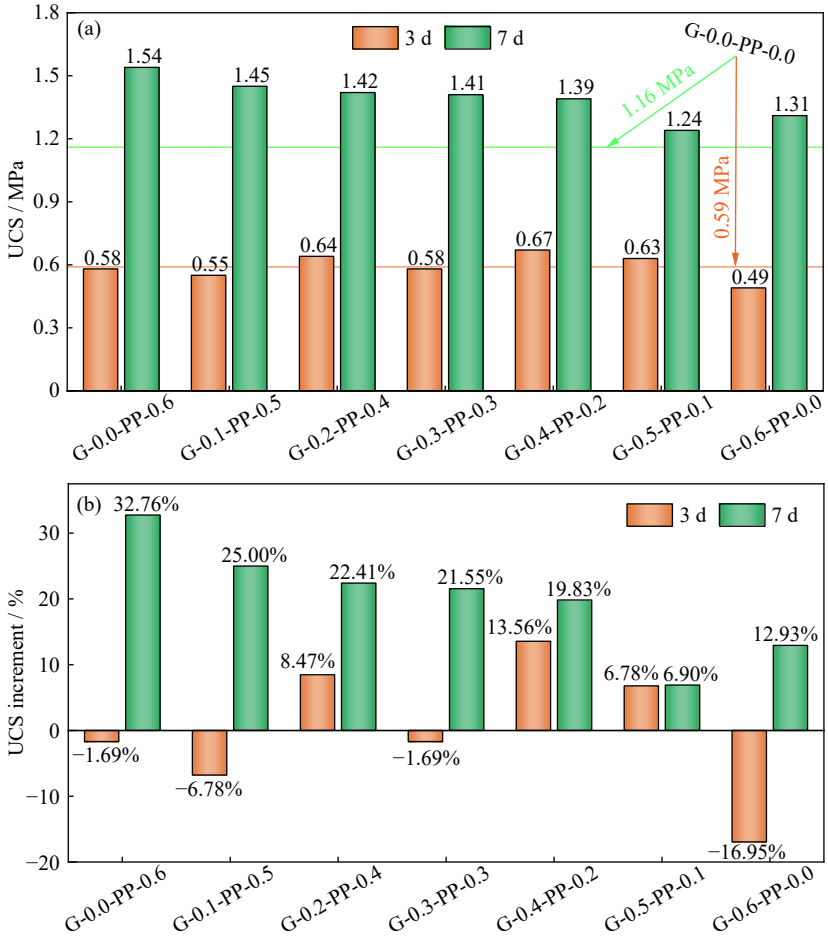

Fig. 4. Relationship among the specimen number: (a) UCS; (b) UCS increment.

were larger than those of the NFRCTB. Among them, the average UCS value of G-0.0-PP-0.6 was the largest (1.54 MPa), and the UCS increment was 32.76%. The average UCS values of the FRCTB specimens increased with the PP fiber content increase. The average UCS values of the FRCTB specimens increased from 1.31 to 1.54 MPa, and the UCS increment increased from 12.93% to 32.76% when the PP content increased from 0.0wt% to 0.6wt%. The results showed that the fibers have a significant strengthening effect on the UCS. The possible reason is that a large number of hydration products, including ettringite and calcium silicate hydrate (C–S–H), were generated, and the bridging effect between the hydration products and fibers was enhanced.

3.2. Effect of fiber content on the peak strain

The relationship among the specimen number, peak strain, and peak strain increment is shown in Fig. 5. All the peak strain values of the FRCTB specimens were larger than those of the NFRCTB. For example, when the curing time is 3 d, the average peak strain values of G-0.0-PP-0.0, G-0.0-PP-0.6, and G-0.6-PP-0.0 were 1.09%, 1.30%, and 4.76%, respectively. Moreover, the peak strain and peak strain increment of the FRCTB specimens increased with the glass fiber content increase. The average peak strain increments of G-0.0-PP-0.6 and G-0.6-PP-0.0 were 19.27% and 336.70% when the curing time was 3 d. However, the peak strain of the glass fiber reinforced CTB decreased with the curing time increase. Taking G-0.1-PP-0.5 as an example, the peak strain values were 2.59% and 1.60% when the curing times were 3 and 7 d, respectively. Moreover, the peak strain values of G-0.6-PP-0.0 were 4.76% and 2.08% when the curing times were 3 and 7 d, respectively.

3.3. Strain development and fracture analysis of the CTB specimens

To show the strain development and fracture analysis of the NFRCTB and FRCTB specimens, the stress and strain curves of the G-0.0-PP-0.0, G-0.6-PP-0.0, and G-0.1-PP-0.5 specimens are shown in Fig. 6. The peak stress of specimens G-0.6-PP-0.0 and G-0.1-PP-0.5 were 1.31 and 1.45 MPa, which were 1.16 and 1.28 times that of specimen G-0.0-PP-0.0 (without reinforcement), respectively. Moreover, the ductility of the FRCTB was clearly better than that of the NFRCTB. To obtain the characteristics of the crack development during the whole loading process, four points A, B, C, and D were considered. The strains in the X and Y directions are represented by ε_x and ε_y, respectively. The evolutions of the strain contour corresponding to the featured points (A–D) at different loading levels obtained by the DIC system during uniaxial compression are shown in Figs. 7–9, respectively.

Fig. 7 shows the development of the strain counter evolution before the peak UCS value. The strain distribution on the

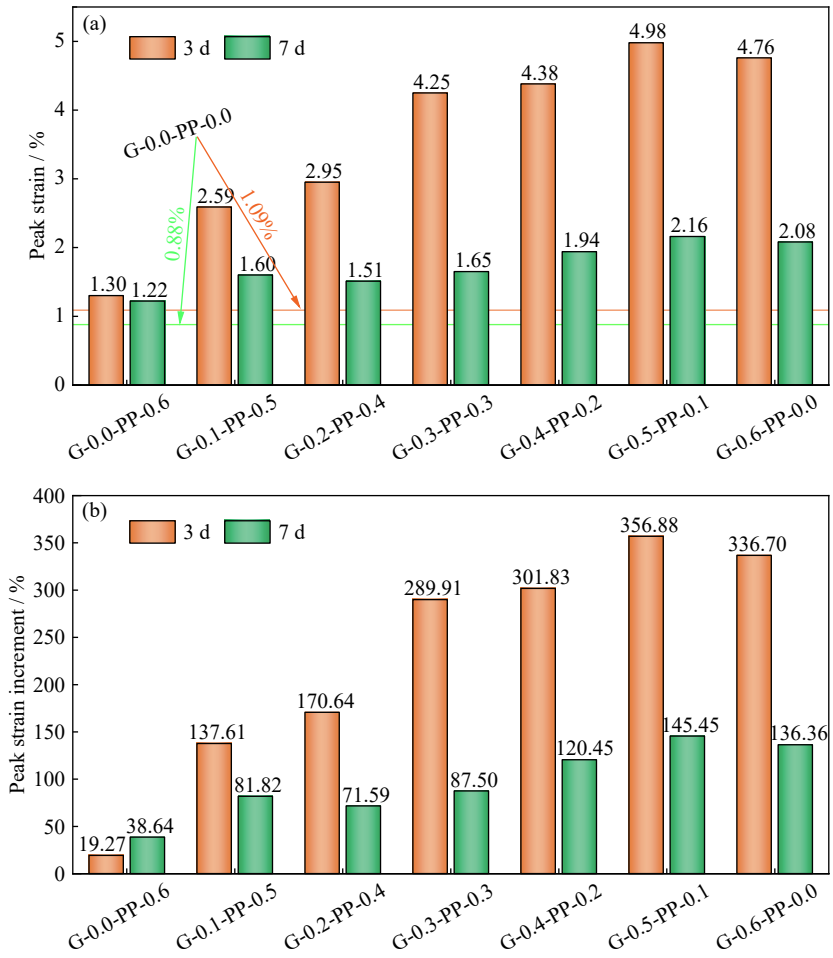

Fig. 5. Bar charts between the peak strain and fiber content: (a) peak strain; (b) peak strain increment.

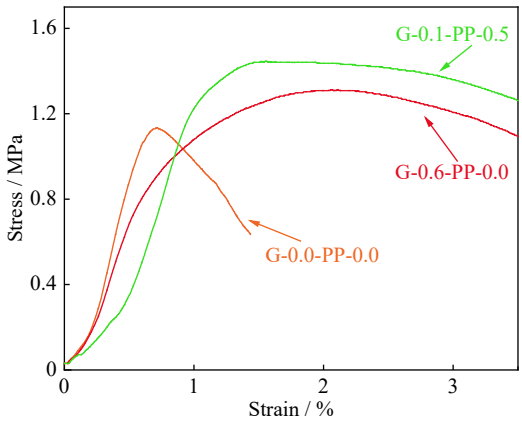

Fig. 6. Strain–stress curves of the CTB specimens at curing time of 7 d.

surface of the G-0.0-PP-0.0 specimen was uniform without clear concentrations at the beginning of the loading. The initial cracks did not substantially develop, as reported by Liu *et al.* [42]. As the load increased (when the stress was less than 0.79 MPa), the cracks on the surface continued to expand, but they were not connected. The corresponding stage was the linear elastic stage in the stress–strain curve. Moreover, as the load continued to increase (when the stress was less than 1.06 MPa), the cracks on the surface continued to expand and penetrate. When the stress exceeded 1.06 MPa, the crack propagation rate accelerated, a large number of main cracks and secondary cracks were generated, and some CTB bulks fell off from the surface of the tested G-0.0-PP-0.0 specimen.

As shown in Figs. 8 and 9, the strain counter development evolutions of the G-0.1-PP-0.5 and G-0.6-PP-0.0 specimens were similar to that of the G-0.0-PP-0.0 specimen. However, the strain in the *X* and *Y* directions corresponding to the peak value of the FRCTB was larger than that of the NFRCTB. For example, the strain values in the *X* and *Y* directions corresponding to the peak strength of the G-0.6-PP-0.0 specimen were 18.652% and 4.696%, respectively, whereas the strains in the *X* and *Y* directions corresponding to the peak strength of the G-0.0-PP-0.0 sample were 2.408% and 0.107%, respectively. Compared with the G-0.0-PP-0.0 specimen, the strain value in the *X* and *Y* directions of G-0.6-PP-0.0 increased by 6.7 and 42.9 times, respectively, which indicated that the additive fiber improved the deformation resistance of the CTB.

Fig. 10 shows the final failure pattern of all the CTB specimens and DIC strain measurement results. The DIC results accurately calibrated the location of the cracks on the surface of the CTB specimens. The failure pattern of the G-0.0-PP-0.0 specimen was mainly tensile failures, and two main cracks parallel to the load direction appeared on the surface. However, cracks parallel and perpendicular to the load direction were observed on the surface of the FRCTB specimens.

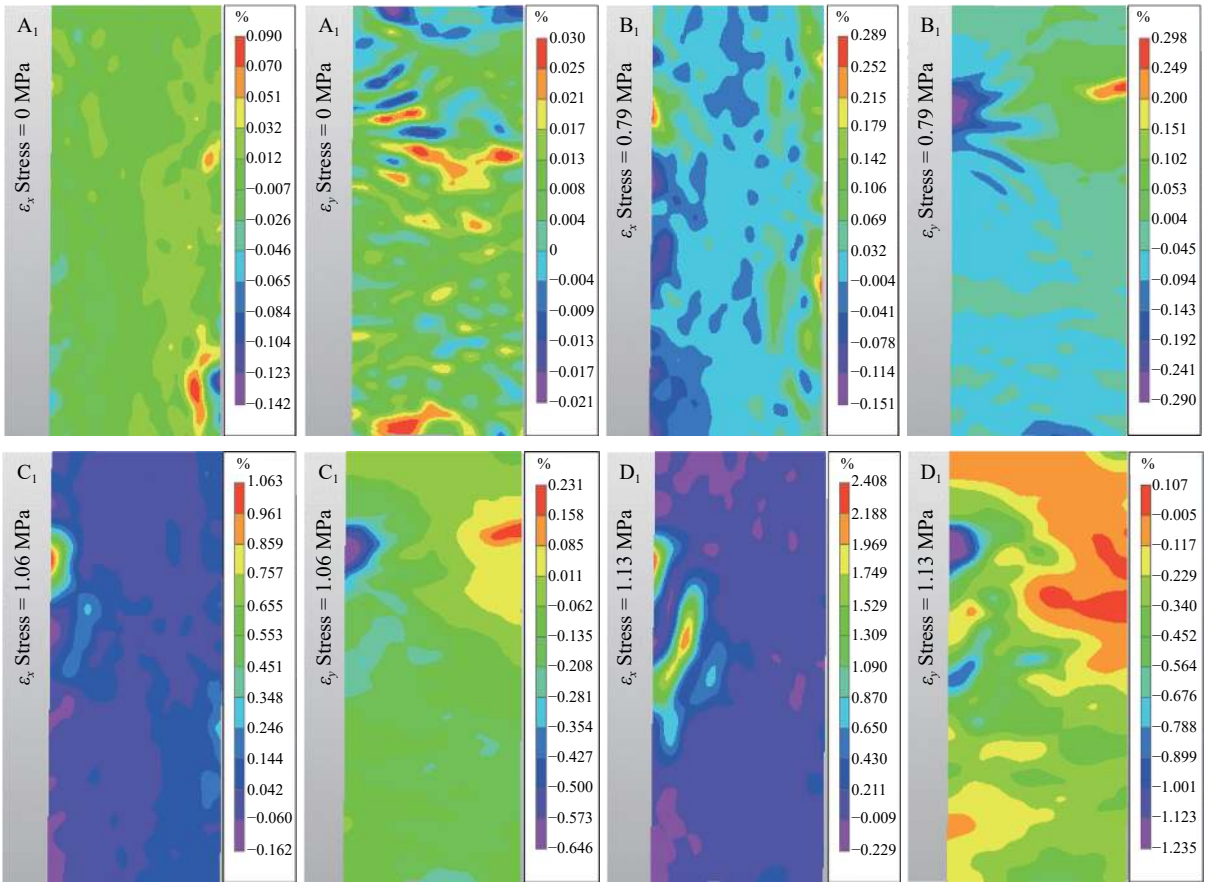

Fig. 7. Full-field strain mappings of the G-0.0-PP-0.0 specimen at points A–D.

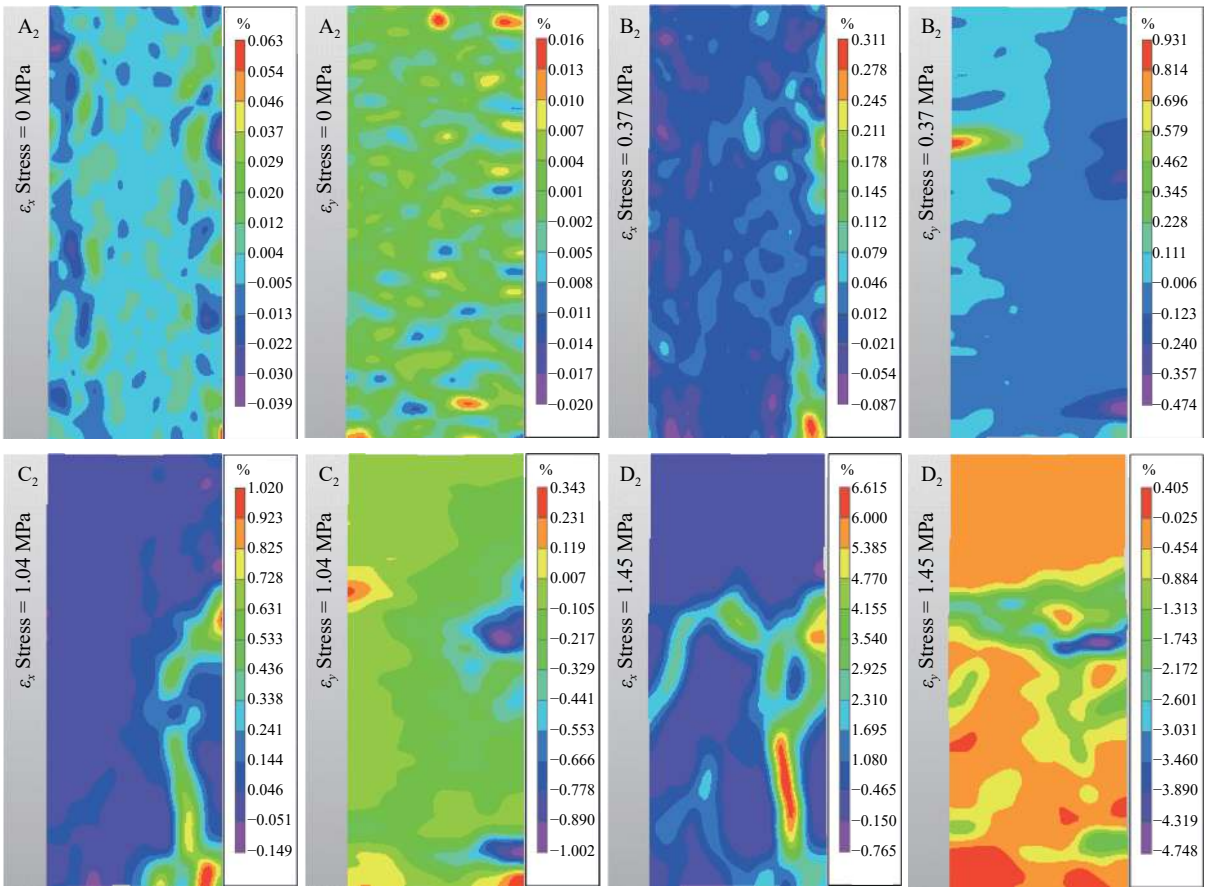

Fig. 8. Full-field strain mappings of the G-0.1-PP-0.5 specimen at points A–D.

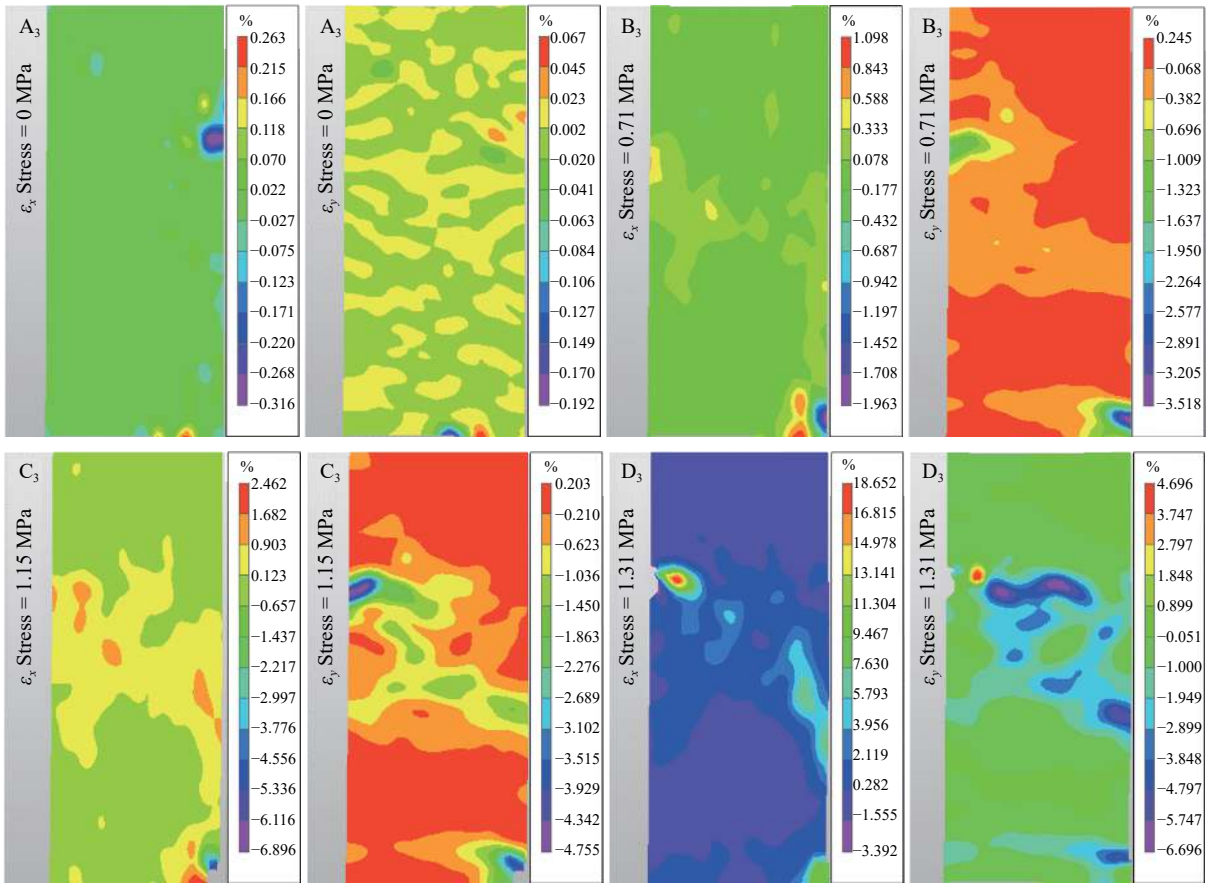

Fig. 9. Full-field strain mappings of the G-0.6-PP-0.0 specimen at points A–D.

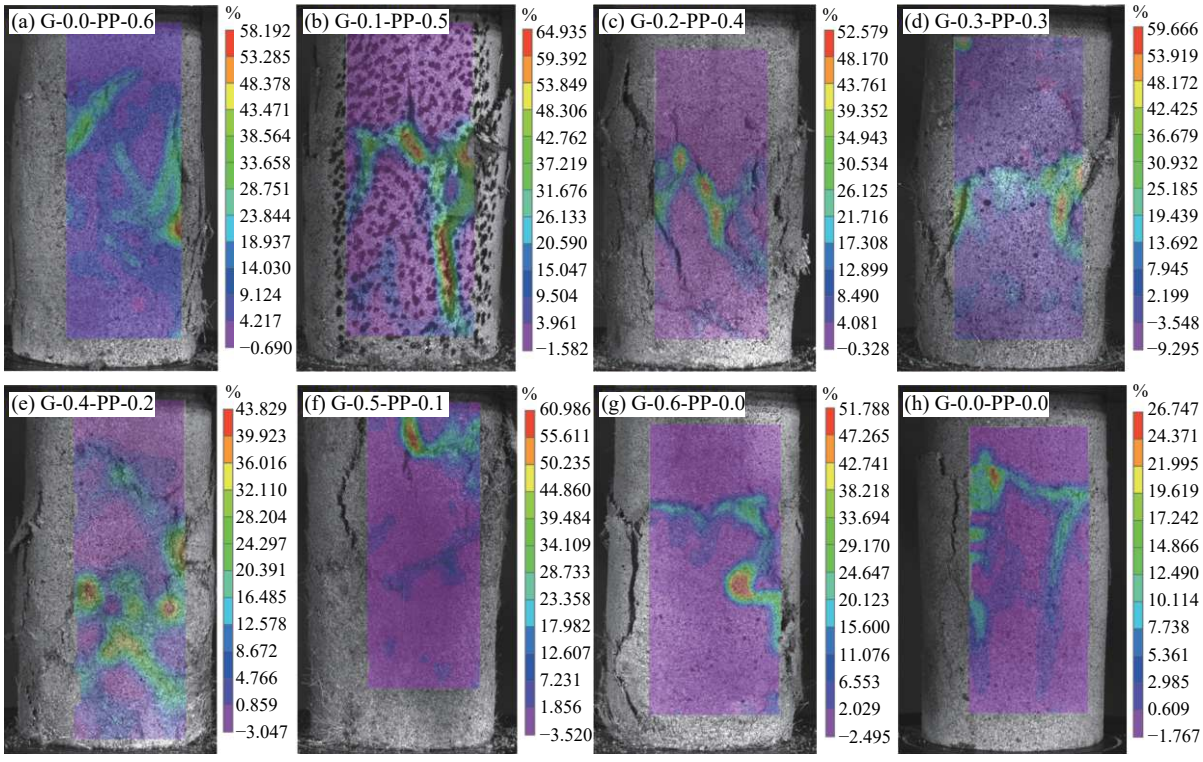

Fig. 10. Strain distribution in the final cracked CTB sample from the DIC.

Thus, the failure patterns were mainly tensile failure and shear failure, and the tensile crack and shear crack intertwined on the surface. Based on the DIC measurement results, the maximum strain values at the location of the crack of the FRCTB were larger than those of the NFRCTB. This result is attributed to the bridging effect of the fiber that limited

the propagation of cracks, thereby improving its resistance to deformation.

3.4. Analysis of the SEM–EDS measurements

In this section, the microstructural characteristics of the FRCTB are investigated. The effect of the interaction of the glass and PP fibers on the mechanical properties of the FRCTB was examined. Fig. 11(a)–(d) show the distribution of the glass and PP fibers on the fracture surface of the failed FRCTB.

As shown in Fig. 11(a), the glass fiber is evenly distributed at the cross-section of the FRCTB, and the diameter (d) of the glass fiber after pulling out is between 18.33 and 23.08 μm. This finding indicates that there is no significant change in the diameter and shape of the glass fiber after being drawn. Moreover, the morphology of the PP fiber at the fracture surface was different from that of the initial shape of the PP fiber. Part of the PP fibers was bent and deformed after being stretched, and the diameter became smaller, with a minimum diameter of 26.88 μm, which indicated that the PP fiber is prone to deformation. In addition, there were some cracked PP fibers on the fracture surface of the FRCTB samples. Fig. 11(b) (Areas 1 and 2) shows the microscopic morphology of the cracked PP fibers. The diameter of the cracked PP fiber became much larger than before, and the largest diameter was 198.65 μm. A large number of hydration products and unhydrated tailings particles were attached to the inner wall of the cracked PP fiber. This phenomenon was possibly related to the poor heat resistance of the PP fiber, which was affected by the exothermic heat of the hydration reaction and caused expansion and cracking. As shown in Fig. 11(c) and (d), there are evident scratches on the surface of the FRCTB samples after the fiber was pulled out. A large number of hydration products were attached to the PP fibers. However, there was only a small amount of hydration products on the surface of the glass fibers, which was relatively smooth. This finding indicates that the reinforcement effect of the PP fiber was better than that of the glass fiber.

The initiation and expansion of the internal cracks were the main reasons for the failure of the CTB. Many studies showed that the essence of the FRCTB strength was achieved by the fiber's inhibitory effect on the crack propagation inside the backfill materials. Fig. 12 shows the microscopic morphology of the internal microcracks of the FRCTB with different fiber combinations. The widths of the microcracks in the FRCTB were larger, which was caused by the bridging effect of the fibers. The hydration products were the main substance connecting the fiber and cemented composite matrix. The fibers on both sides of the connecting cracks were subjected to friction to inhibit the crack propagation during the crack expansion process, which led to the excessive damage of the FTCTB from brittle failure to ductile failure. Fig. 12(c) (Areas 1, 2, and 3) also shows that the width of the cracks connected by the PP fiber was larger than those connected by the glass fiber.

Fig. 13 shows the distribution of the main elements in the

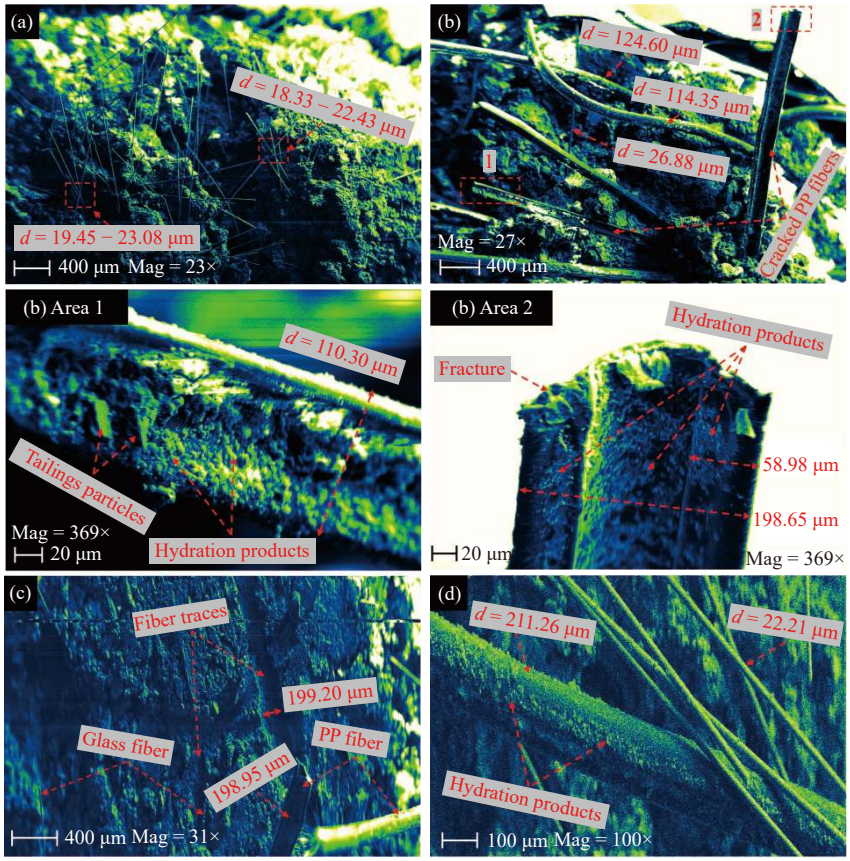

Fig. 11. Distribution of the glass and PP fibers on the fracture surface of the CTB: (a) G-0.6-PP-0.0; (b) G-0.0-PP-0.6; (c) G-0.2-PP-0.4; (d) G-4.0-PP-0.2.

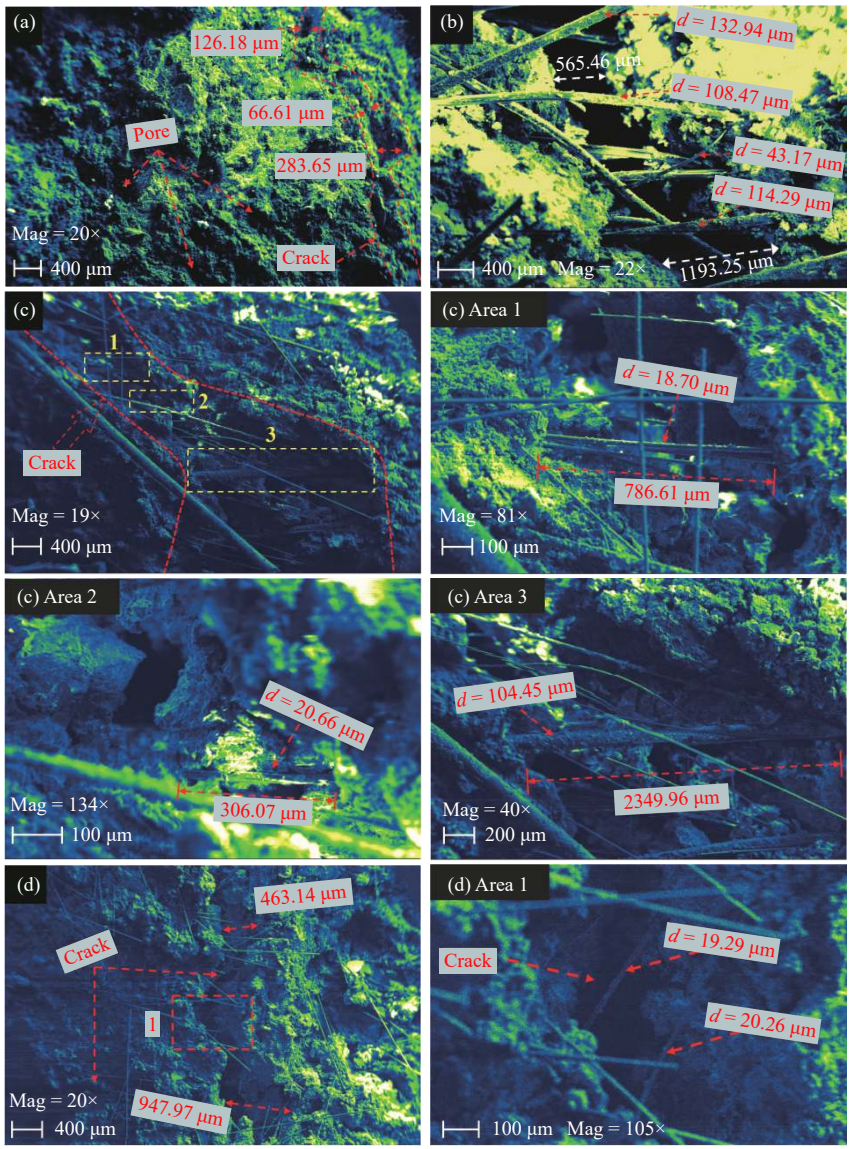

Fig. 12. SEM micrographs of the CTB crack: (a) G-0.0-PP-0.0; (b) G-0.0-PP-0.6; (c) G-0.3-PP-0.3; (d) G-0.6-PP-0.0.

G-0.0-PP-0.0 specimen. The microscopic image shows that a large amount of gelling substances were attached to the surface of the tailings particles. Generally, the O, Ca, Si, Al, K, Mg, and other elements were uniformly distributed on the surface of the tested sample. However, the O, Ca, Si, and Al were dense in the hydration products. The content of hydration products was directly related to the strength of the CTB. Fig. 14 shows the EDS value of the hydration product in the CTB. The main hydration products were needle-shaped and sheet-shaped ettringite (AFt: $3CaO{\cdot}Al_2O_3{\cdot}3CaSO_4{\cdot}32H_2O$)

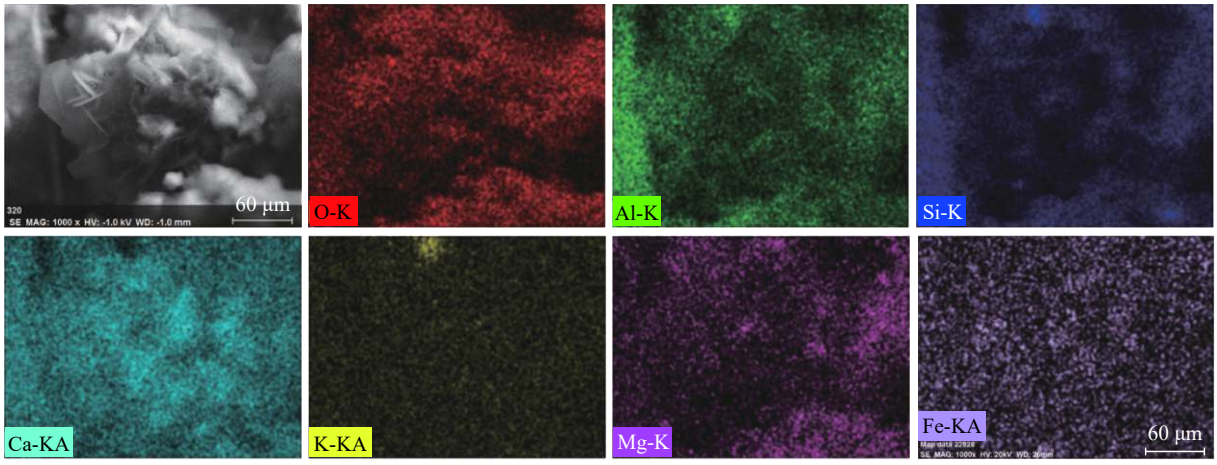

Fig. 13. Main element mapping distributions of the G-0.0-PP-0.0 CTB sample.

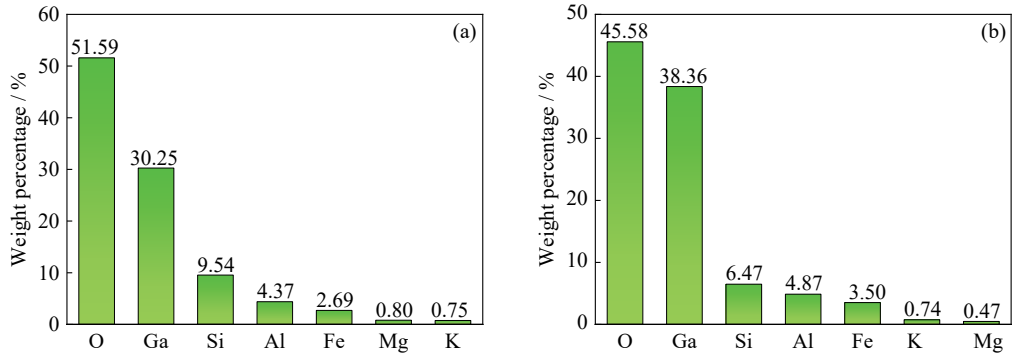

Fig. 14. EDS values of hydration products (G-0.0-PP-0.0): (a) C–S–H; (b) AFt.

and floc-shaped C–S–H gels. The mass fractions of O, Ca, Si, and Al in the hydration products were relatively large, and these elements were the main elements in AFt and C–S–H.

4. Conclusions

In this study, a series of experimental tests, including uniaxial compression, failure evolution, and microstructural characteristics of CTB, was conducted to explore the mechanical behavior of combined PP and glass fiber-reinforced CTB. The main conclusions were drawn as follows.

(1) The UCS of the FRCTB was larger than that of the NFRCTB. Adding fibers can increase the UCS values of the CTB by 6.90% to 32.76%. The UCS value of the FRCTB increased with the PP fiber content increase. Moreover, the reinforcement effect of the PP fiber on the CTB was better than that of the glass fiber. The ductility of the FRCTB was significantly better than that of the NFRCTB. The addition of fiber could increase the peak strain of the FRCTB by 0.39% to 1.45%, and the peak strain of the FRCTB increased with the glass fiber content increase.

(2) The cracks of the CTB were mainly generated at the stress concentration position of the strain cloud counter. The failure pattern of the NFRCTB was a tensile failure, and the failure pattern of the FRCTB was coupled with tensile and shear failure. The hydration product was the main substance that connects the fiber and CTB matrix. The addition of fiber effectively inhibited the propagation of cracks, and the bridging effect of cracks by the fiber effectively improved the mechanical properties of the FRCTB.

The addition of combined fibers improved the mechanical strength of the CTB and increased the ductility. The obtained results are valuable for the development and field application of the technology of the CTB. However, the reinforcement mechanism of the combined fibers, pipeline transportation of the FRCTB slurry, and on-site industrial application are all key problems that need to be considered in the future. In future research, more experimental methods will be used to study these issues in depth.

Acknowledgements

This work was financially supported by the National Natural Science Foundation of China (No. 51804017), the Fundamental Research Funds for Central Universities, China (No. FRF-TP-20-001A2), and the State Key Laboratory of Silicate Materials for Architectures（Wuhan University of Technology）(No. SYSJJ2021-04).

Conflict of Interest

The authors declare that they have no known competing financial interests or personal relationships that could have appeared to influence the work reported in this paper.

References

[1] M.J. Raffaldi, J.B. Seymour, J. Richardson, E. Zahl, and M. Board, Cemented paste backfill geomechanics at a narrow-vein underhand cut-and-fill mine, *Rock Mech. Rock Eng.*, 52(2019), No. 12, p. 4925.

[2] L. Liu, P. Zhou, Y. Feng, B. Zhang, and K.I. Song, Quantitative investigation on micro-parameters of cemented paste backfill and its sensitivity analysis, *J. Cent. South Univ.*, 27(2020), No. 1, p. 267.

[3] Q.S. Chen, S.Y. Sun, Y.K. Liu, C.C. Qi, H.B. Zhou, and Q.L. Zhang, Immobilization and leaching characteristics of fluoride from phosphogypsum-based cemented paste backfill, *Int. J. Miner. Metall. Mater.*, 28(2021), No. 9, p. 1440.

[4] L. Liu, J. Xin, C. Huan, Y.J. Zhao, X. Fan, L.J. Guo, and K.I. Song, Effect of curing time on the mesoscopic parameters of cemented paste backfill simulated using the particle flow code technique, *Int. J. Miner. Metall. Mater.*, 28(2021), No. 4, p. 590.

[5] D. Wu, R.K. Zhao, C.W. Xie, and S. Liu, Effect of curing humidity on performance of cemented paste backfill, *Int. J. Miner. Metall. Mater.*, 27(2020), No. 8, p. 1046.

[6] D.L. Wang, Q.L. Zhang, Q.S. Chen, C.C. Qi, Y. Feng, and C.C. Xiao, Temperature variation characteristics in flocculation settlement of tailings and its mechanism, *Int. J. Miner. Metall. Mater.*, 27(2020), No. 11, p. 1438.

[7] A. Antonova, M. Eik, V. Jokinen, and J. Puttonen, Effect of the roughness of steel fibre surface on its wettability and the cement paste close to fibre surface, *Constr. Build. Mater.*, 289(2021), art. No. 123139.

[8] A.F. Guo, Z.H. Sun, and J. Satyavolu, Impact of modified kenaf fibers on shrinkage and cracking of cement pastes, *Constr. Build. Mater.*, 264(2020), art. No. 120230.

[9] J.J. Li, S. Cao, and E. Yilmaz, Characterization of macro mechanical properties and microstructures of cement-based composites prepared from fly ash, gypsum and steel slag, *Minerals*, 12(2022), No. 1, art. No. 6.

[10] O. Hamdaoui, O. Limam, L. Ibos, and A. Mazioud, Thermal and mechanical properties of hardened cement paste reinforced

with *Posidonia-Oceanica* natural fibers, *Constr. Build. Mater.*, 269(2021), art. No. 121339.
[11] L. Yang, E. Yilmaz, J.W. Li, H. Liu, and H.Q. Jiang, Effect of superplasticizer type and dosage on fluidity and strength behavior of cemented tailings backfill with different solid contents, *Constr. Build. Mater.*, 187(2018), p. 290.
[12] J.J. Li, E. Yilmaz, and S. Cao, Influence of industrial solid waste as filling material on mechanical and microstructural characteristics of cementitious backfills, *Constr. Build. Mater.*, 299(2021), art. No. 124288.
[13] M. Szeląg, Evaluation of cracking patterns of cement paste containing polypropylene fibers, *Compos. Struct.*, 220(2019), p. 402.
[14] X. Chen, X.Z. Shi, J. Zhou, Q.S. Chen, E.M. Li, and X.H. Du, Compressive behavior and microstructural properties of tailings polypropylene fibre-reinforced cemented paste backfill, *Constr. Build. Mater.*, 190(2018), p. 211.
[15] M. Hambach and D. Volkmer, Properties of 3D-printed fiber-reinforced Portland cement paste, *Cem. Concr. Compos.*, 79(2017), p. 62.
[16] D.Y. Wei, C.F. Du, Y.F. Lin, and B.M. Chang, Impact factors of hydration heat of cemented tailings backfill based on multi-index optimization, *Case Stud. Therm. Eng.*, 18(2020), art. No. 100601.
[17] C.C. Qi, A. Fourie, Q.S. Chen, and Q.L. Zhang, A strength prediction model using artificial intelligence for recycling waste tailings as cemented paste backfill, *J. Cleaner Prod.*, 183(2018), p. 566.
[18] M. Fall, J.C. Célestin, M. Pokharel, and M. Touré, A contribution to understanding the effects of curing temperature on the mechanical properties of mine cemented tailings backfill, *Eng. Geol.*, 114(2010), No. 3-4, p. 397.
[19] H.Q. Jiang and M. Fall, Yield stress and strength of saline cemented tailings in sub-zero environments: Portland cement paste backfill, *Int. J. Miner. Process.*, 160(2017), p. 68.
[20] M. Fall and M. Pokharel, Coupled effects of sulphate and temperature on the strength development of cemented tailings backfills: Portland cement-paste backfill, *Cem. Concr. Compos.*, 32(2010), No. 10, p. 819.
[21] D. Zheng, W.D. Song, J.X. Fu, G.L. Xue, J.J. Li, and S. Cao, Research on mechanical characteristics, fractal dimension and internal structure of fiber reinforced concrete under uniaxial compression, *Constr. Build. Mater.*, 258(2020), art. No. 120351.
[22] Z.Q. Huang, E. Yilmaz, and S. Cao, Analysis of strength and microstructural characteristics of mine backfills containing fly ash and desulfurized gypsum, *Minerals*, 11(2021), No. 4, art. No. 409.
[23] D. Zheng, W.D. Song, S. Cao, J.J. Li, and L.J. Sun, Investigation on dynamical mechanics, energy dissipation, and microstructural characteristics of cemented tailings backfill under SHPB tests, *Minerals*, 11(2021), No. 5, art. No. 542.
[24] Y.Y. Tan, E. Davide, Y.C. Zhou, W.D. Song, and X. Meng, Long-term mechanical behavior and characteristics of cemented tailings backfill through impact loading, *Int. J. Miner. Metall. Mater.*, 27(2020), No. 2, p. 140.
[25] J.R. Zheng, X.X. Sun, L.J. Guo, S.M. Zhang, and J.Y. Chen, Strength and hydration products of cemented paste backfill from sulphide-rich tailings using reactive MgO-activated slag as a binder, *Constr. Build. Mater.*, 203(2019), p. 111.
[26] D. Zheng, W.D. Song, Y.Y. Tan, S. Cao, Z.L. Yang, and L.J. Sun, Fractal and microscopic quantitative characterization of unclassified tailings flocs, *Int. J. Miner. Metall. Mater.*, 28(2021), No. 9, p. 1429.
[27] Y.L. Zhao, Z.Y. Ma, J.P. Qiu, X.G. Sun, and X.W. Gu, Experimental study on the utilization of steel slag for cemented ultra-fine tailings backfill, *Powder Technol.*, 375(2020), p. 284.
[28] L. Liu, J. Xin, C. Huan, C.C. Qi, W.W. Zhou, and K.I. Song, Pore and strength characteristics of cemented paste backfill using sulphide tailings: Effect of sulphur content, *Constr. Build. Mater.*, 237(2020), art. No. 117452.
[29] Q.S. Chen, Q.L. Zhang, A. Fourie, and C. Xin, Utilization of phosphogypsum and phosphate tailings for cemented paste backfill, *J. Environ. Manage.*, 201(2017), p. 19.
[30] G.L. Xue, E. Yilmaz, G.R. Feng, and S. Cao, Bending behavior and failure mode of cemented tailings backfill composites incorporating different fibers for sustainable construction, *Constr. Build. Mater.*, 289(2021), art. No. 123163.
[31] S. Cao, E. Yilmaz, Z.Y. Yin, G.L. Xue, W.D. Song, and L.J. Sun, CT scanning of internal crack mechanism and strength behavior of cement-fiber-tailings matrix composites, *Cem. Concr. Compos.*, 116(2021), art. No. 103865.
[32] G.L. Xue, E. Yilmaz, G.R. Feng, S. Cao, and L.J. Sun, Reinforcement effect of polypropylene fiber on dynamic properties of cemented tailings backfill under SHPB impact loading, *Constr. Build. Mater.*, 279(2021), art. No. 122417.
[33] G.L. Xue, E. Yilmaz, W.D. Song, and S. Cao, Fiber length effect on strength properties of polypropylene fiber reinforced cemented tailings backfill specimens with different sizes, *Constr. Build. Mater.*, 241(2020), art. No. 118113.
[34] W.B. Xu, Q.L. Li, and Y.L. Zhang, Influence of temperature on compressive strength, microstructure properties and failure pattern of fiber-reinforced cemented tailings backfill, *Constr. Build. Mater.*, 222(2019), p. 776.
[35] F. Xu, S.L. Wang, T. Li, B. Liu, B.B. Li, and Y. Zhou, Mechanical properties and pore structure of recycled aggregate concrete made with iron ore tailings and polypropylene fibers, *J. Build. Eng.*, 33(2021), art. No. 101572.
[36] S. Cao, D. Zheng, E. Yilmaz, Z.Y. Yin, G.L. Xue, and F.D. Yang, Strength development and microstructure characteristics of artificial concrete pillar considering fiber type and content effects, *Constr. Build. Mater.*, 256(2020), art. No. 119408.
[37] Y.D. Gan, H.Z. Zhang, Y. Zhang, Y.D. Xu, E. Schlangen, K.van Breugel, and B. Šavija, Experimental study of flexural fatigue behaviour of cement paste at the microscale, *Int. J. Fatigue*, 151(2021), art. No. 106378.
[38] B. Liu, J.K. Zhou, X.Y. Wen, X. Hu, and Z.H. Deng, Mechanical properties and constitutive model of carbon fiber reinforced coral concrete under uniaxial compression, *Constr. Build. Mater.*, 263(2020), art. No. 120649.
[39] S. Chakilam and L. Cui, Effect of polypropylene fiber content and fiber length on the saturated hydraulic conductivity of hydrating cemented paste backfill, *Constr. Build. Mater.*, 262(2020), art. No. 120854.
[40] Y.Y. Wang, Z.Q. Yu, and H.W. Wang, Experimental investigation on some performance of rubber fiber modified cemented paste backfill, *Constr. Build. Mater.*, 271(2021), art. No. 121586.
[41] X. Chen, X.Z. Shi, J. Zhou, Z. Yu, and P.S. Huang, Determination of mechanical, flowability, and microstructural properties of cemented tailings backfill containing rice straw, *Constr. Build. Mater.*, 246(2020), art. No. 118520.
[42] B.W. Liu, F. Yue, B. Chen, X.Y. Man, L. Chen, and S. Jaisee, Study on bond performance, flexural and crack extension behavior of base concrete prisms strengthen with strain-hardening cementitious composites (SHCC) using DIC technology, *Constr. Build. Mater.*, 251(2020), art. No. 119035.